AGU PUBLICATIONS

JGR

Journal of Geophysical Research: Solid Earth

RESEARCH ARTICLE
10.1002/2016JB012886

Key Points:
- Structural asperity focusing locking and coseismic slip
- Coseismic slip matches previously recognized locked patch
- Key role of interface topography on our interpretation of the seismic cycle along megathrust

Supporting Information:
- Supporting Information S1

Correspondence to:
C. Kyriakopoulos,
christos@ucr.edu

Citation:
Kyriakopoulos, C., and A. V. Newman (2016), Structural asperity focusing locking and earthquake slip along the Nicoya megathrust, Costa Rica, *J. Geophys. Res. Solid Earth*, *121*, doi:10.1002/2016JB012886.

Received 9 FEB 2016
Accepted 29 JUN 2016
Accepted article online 4 JUL 2016

Structural asperity focusing locking and earthquake slip along the Nicoya megathrust, Costa Rica

C. Kyriakopoulos[1] and A. V. Newman[2]

[1]Department of Earth Sciences, Geology Building, University of California, Riverside, California, USA, [2]School of Earth and Atmospheric Sciences, Georgia Institute of Technology, Atlanta, Georgia, USA

Abstract On 5 September 2012, a moment magnitude 7.6 earthquake occurred along the locked megathrust interface directly beneath the Nicoya Peninsula in Costa Rica. The event was anticipated given the history of frequent large earthquakes and recent GPS results. Strain accumulation observed before and coseismic slip observed during the earthquake create a novel and important data set, offering a unique look at the strain and locking behavior around a large megathrust environment. Given this geodetic data, and a newly developed regional 3-D subduction interface, we develop a regionally appropriate finite element model to evaluate the role of interface topography in generating interseismic locking and ultimately coseismic slip following the 2012 earthquake. We find that the interface is most strongly coupled in a patch immediately beneath the central portion of Nicoya in an area where a topographic high in the downgoing Cocos Plate is resisting further subduction. This zone is the dominant slip environment in the 2012 earthquake. Reevaluation of the interseismic locking over 62 years before the most recent event finds that the total accumulated moment potential ($M_0 = 3.48 \times 10^{20}$ N m) well matches the total moment release in the 2012 rupture found here ($M_0 = 3.73 \times 10^{20}$ N m, M_w 7.68), with rupture extending to the SE outside of the strongly locked region, possibly as early afterslip. In contrast to a prior study, little locking is required immediately offshore Nicoya—a conclusion important for understanding the rupture area of the 2012 event, regional tsunami potential, and relation with regionally observed shallow slow-slip events.

1. Introduction

A high and unusual number of subduction earthquakes marked the past decade. At least five events moment magnitude, $M_w > 8.5$, have rocked the populations of the coastal areas of Indonesia, Chile, and Japan. In the particular case of the Japanese and Indonesian earthquakes, the catastrophic potential was primarily expressed through the generation of 20 m tsunami waves that devastated the coastal landscape and caused the death of tens of thousands of people. The effects of these earthquakes were felt not only in the area near the hypocenter but also in remote areas hundreds or even thousands of kilometers away. For example, the state of California was hit by the 2011 Tohoku-oki tsunami as a consequence of the waves traveling the length of the Pacific Ocean. As a first-order approximation, we can say that the catastrophic potential of such events depends primarily on the quantity of the seismic moment accumulated during the interseismic period (tens to hundreds of years) and subsequently released during a megathrust earthquake (over tens to hundreds of seconds). We now have the possibility to observe part of the deformation associated with the late interseismic period along major subduction zones using land-based high-precision GPS sensors. Although these observations are only the free-surface expression of the interseismic fault motion, they allow us to estimate the rate of accumulation of seismic moment along the fault interface.

Measuring the interseismic motion is not enough for a complete characterization of the fault system. Beyond the observation of the interseismic deformation, analysis of the prevailing factors that control the accumulation of seismic moment along subduction zones is necessary. For example, the topography of the subducting plate interface has been suggested to act as a mechanical regulator during large interplate earthquakes [*Kanamori*, 1986]. Similarly, interface complexities may act as mechanically strong asperities, accumulating elastic strain during the interseismic period and finally becoming the site of rupture initiation in megathrust events [*Kanamori*, 1986]. The role of interface topography is not unique, in that the only detection of a subducted seamount (or any geometric protuberance) does not necessarily indicate the presence of a seismic asperity. Other factors, such as lithologic frictional properties [*Marone*, 1998; *Ikari et al*., 2013] or the presence of fluids along the interface, may modify the seismic "character" of an individual fault patch. For example,

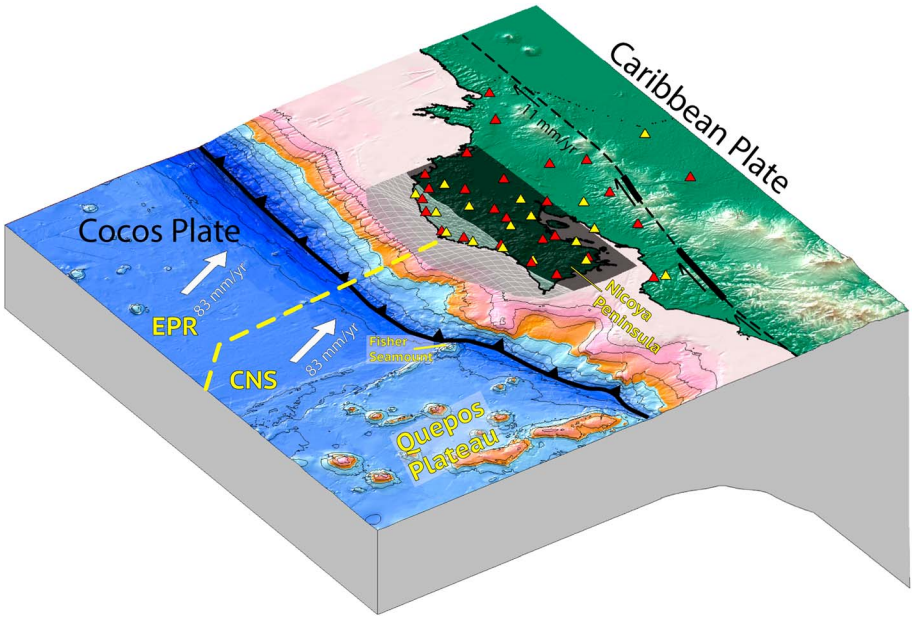

Figure 1. Perspective view of the tectonic setting surrounding the Nicoya Peninsula of Costa Rica. Offshore Nicoya, the Cocos plate descends beneath the Caribbean at approximately 83 mm/yr (white vectors) [*DeMets et al.*, 2010]. A transparency window reveals the geometric irregularity of the slab surface (gray mesh with white grid lines) beneath the Nicoya Peninsula [*Kyriakopoulos et al.*, 2015]. Continuous and campaign GPS stations used in this study are highlighted with yellow and red triangles, respectively. The subducting plate is a combination of two crusts generated at the East Pacific Rise (EPR) and the Cocos-Nazca Spreading center (CNS), with the mapped seaward and downdip projection of the EPR-CNS transition marked with a yellow dashed line [*Barckhausen et al.*, 2001]. The Quepos plateau, subducting to the south of Nicoya, is dominated by seamounts, including the Fisher seamount chain. The Nicoya Peninsula and adjacent land to the west of the volcanic range exhibit approximately 11 mm/yr of northwest sliver transport [*Feng et al.*, 2012]. The location is partially constrained by mapped faults (thick black lines) [*Montero et al.*, 1998] and inferred through interseismic GPS data and geomorphic structures (dashed line).

high-pressure fluids originated from the dehydration of the subducted sediments may modify the effect of what initially appears to be a strong mechanical barrier by reducing the fault normal stress and thus decreasing the interplate coupling [*Wang and Bilek*, 2011]. This will eventually lead to aseismic motion along the plate interface near the seamount region inhibiting future coseismic slip [*Mochizuki et al.*, 2008]. Recently, *Yang et al.* [2013] used dynamic rupture propagation models to show that subducted seamounts near the nucleation area of an earthquake may act as barriers to rupture, limiting the ultimate size of an event.

1.1. The Nicoya Peninsula

Like the majority of Central America, the Nicoya Peninsula consists primarily of uplifted oceanic crust but sits geographically closer to the trench than most places on Earth (Figure 1). Here the peninsula extends 80 km seaward from the regional coastline and is only 60 km from the trench, sitting directly over most of the seismogenic component of the subduction megathrust and thus allowing for detailed land-based geophysical studies. At Nicoya, the Cocos plate subducts obliquely beneath the Caribbean plate at approximately 83 mm/yr [*DeMets et al.*, 2010], driving midmagnitude 7 earthquakes there approximately every 50 years [*Protti et al.*, 2001]. While frequently modeled as a planar or curved two-dimensional interface [e.g., *Norabuena et al.*, 2004; *Feng et al.*, 2012; *Protti et al.*, 2014; *Xue et al.*, 2015], the subduction megathrust beneath Nicoya appears extremely irregular [e.g., *Newman et al.*, 2002; *DeShon et al.*, 2006], resulting from both along-strike changes in the downgoing crustal material and the existence of seamounts. Along strike, the subducting crust transitions from material generated at the trench-parallel East Pacific Rise (EPR) in the northwest to crust generated along the approximately trench-normal Cocos-Nazca Spreading center (CNS) in the southeast [*Barckhausen et al.*, 2001]. Just to the south of Nicoya, the downgoing CNS crust changes again due to a plate rotation, with the newer southern crust remaining much higher, as the Quepos Plateau (Figure 1). This first transition from EPR to CNS crust corresponds with a visible suture that can be observed both in the bathymetry offshore and in the microseismicity beneath Nicoya [*Newman et al.*, 2002]. The microseismicity beneath Nicoya and surrounding area was recently used to describe the megathrust interface,

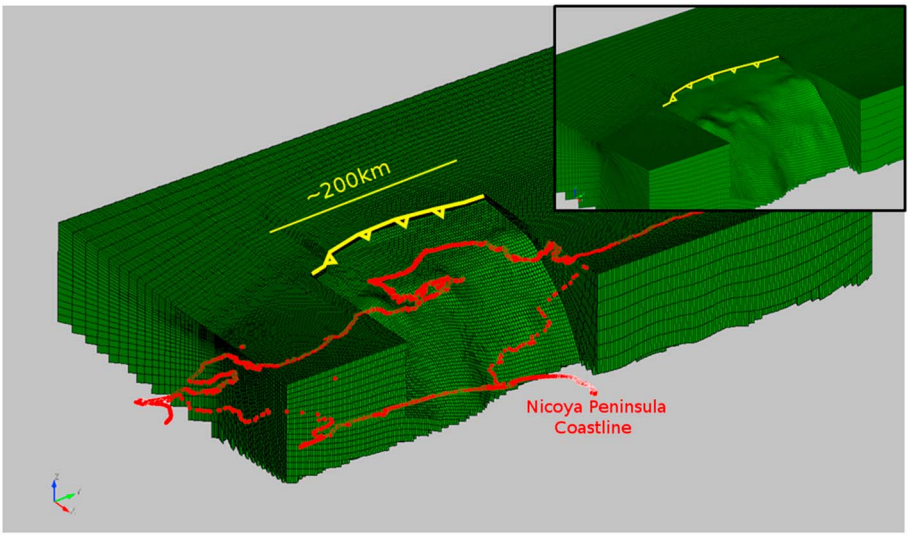

Figure 2. Finite element model for the Nicoya, Costa Rica, subduction zone. The model is defined by the 3-D plate interface geometry along the Nicoya segment of the Middle America Trench subduction zone [*Kyriakopoulos et al*., 2015] and is shown in its entirety in Figure S1. The inset is an uncluttered reproduction of the Nicoya interface. The model is composed of more than two million hexahedral elements, with increased density (~2.5 km nominal node spacing) in the ~200 km surrounding the Nicoya interface. The red dots highlight the Costa Rican and southern Nicaraguan coastlines.

which includes both a sharp transition at the EPR-CNS suture and large-scale undulations farther south, corresponding to the subduction of the continuation of the Fisher Seamount Chain [*Kyriakopoulos et al*., 2015]. It is the first feature, the sharp transition associated with the EPR-CNS transition, that is of primary concern in this study as it is in the center of a complex interseismic locked zone imaged in *Feng et al*. [2012] and in the largest slip zone during a large earthquake that occurred in September 2012 [*Yue et al*., 2013; *Protti et al*., 2014].

1.2. The Nicoya Earthquake

The 5 September 2012 M_w 7.6 earthquake was imaged by a combination of seismic data and real-time GPS [*Yue et al*., 2013], and from the entirety of regional continuous and campaign GPS collected within the first days following *Protti et al*. [2014]. The event is primarily a thrust earthquake directly beneath the Nicoya Peninsula (hereafter called the Nicoya earthquake). Because the 2012 Nicoya earthquake occurred directly over the EPR-CNS suture and in the previously determined locked patch below the dense geophysical network, it provides a unique opportunity to evaluate how locking transitions from late interseismic locking to coseismic slip, and how this is affected by structural complexity in the interface.

2. Modeling

In this study, we simulate the interseismic and coseismic deformation along the Nicoya Peninsula and surrounding area using the slab topography model of *Kyriakopoulos et al*. [2015], in order to determine whether the sharp changes in the interface geometry act to focus or prohibit locking and earthquake rupture. To model the geometry, we solve for elastic deformation using the finite element method (FEM), which allows for separate numerical calculations of deformation across a discretized domain composed of nodes and cells (elements).

2.1. Model Geometry and Mesh

To develop the FEM model geometry and mesh (Figure 2), we imported the geometry of *Kyriakopoulos et al*. [2015] into the software package, CUBIT (https://cubit.sandia.gov). Since we aim to characterize the deformation pattern of both interseismic and coseismic phases along the fault surface, it is necessary to precisely define geometric features along the subduction interface. To do so, we developed a mesh that is both large in spatial dimensions (to minimize boundary effects) and with high element density near the simulated rupture interface. The total model dimensions are $3600 \times 3600 \times 600$ km with the slab interface located along

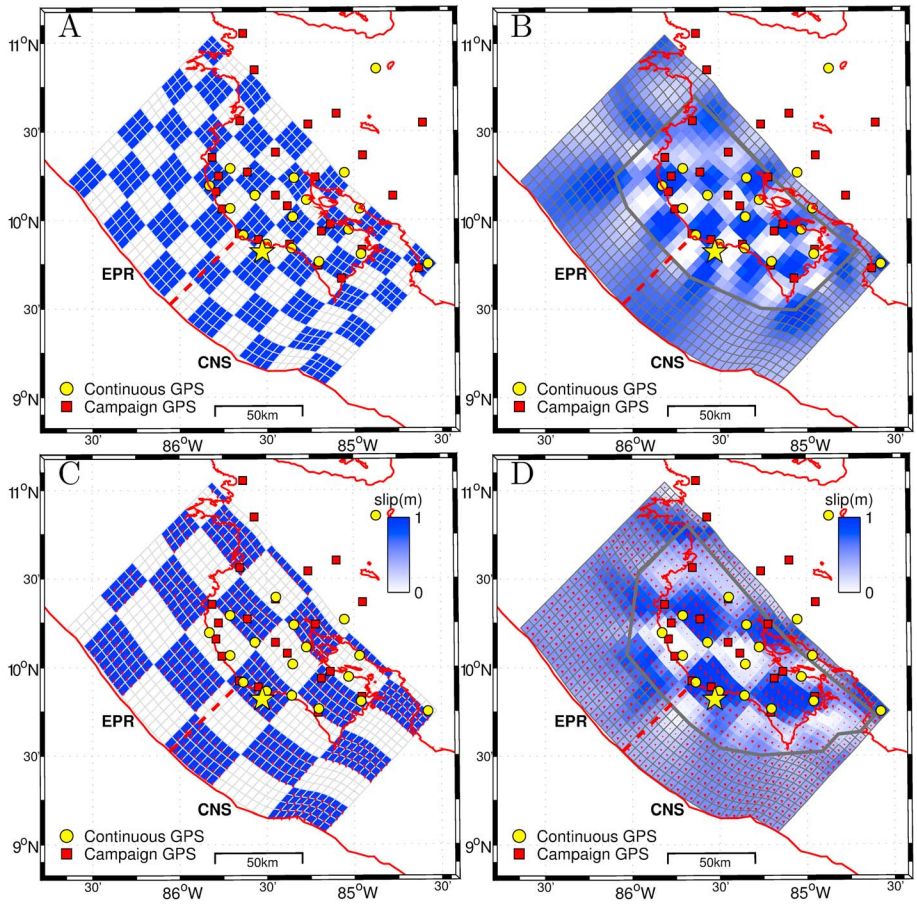

Figure 3. Model resolution tests. (a) Input interseismic velocity model (4 × 3 element groups with 0 and 78.5 mm/yr of back slip) used for the spatial resolution test of the GPS network. (b) Inverted interface back slip rates using predicted surface velocities from Figure 3a for the existing GPS network. (c) Input coseismic slip model (8 × 4 element groups with 0 and 1 m of slip). (d) Inverted interface slip using predicted surface displacements from Figure 3c for the GPS network configuration at the time of the 2012 earthquake. The thick gray polygons in Figures 3b and 3d enclose the limits of the highly resolvable area beneath Nicoya for the periods of interest. The red dashed line marks the transition between the subducted extension of the East Pacific Rise (EPR) and Cocos-Nazca Spreading center (CNS) crusts, while the Nicoya Peninsula and Middle America Trench are marked with red solid lines.

the center of the domain. The final model comprises more than 2.5 million hexahedral elements in a structured mesh. The characteristic length for elements is approximately 2.5 km near the slab interface, progressively increasing to approximately 200 km at the lateral and bottom boundaries of the model.

The interface separating the subducting slab from the overriding plate in our model occurs along an about 700 km long fault extending from southern Costa Rica through Northern Nicaragua. The rupture interface is partitioned into 4389 coincident node pairs (133 × 33 fault patches of approximately 5 × 5 km in area) to allow for a distribution of coseismic slip or locking, which will be estimated from geodetic data using linear inverse methods. In this study, our modeling of locking and slip behavior is limited to the fault below and surrounding the Nicoya Peninsula approximately 200 km in length and consisting of 43 (along-strike) × 21 (along-dip) pairs of coincident nodes (patches). Because the interface has an irregular shape, the maximum depth reached by the fault varies along strike from 36 km at the southeast corner (beneath the town of Jaco) to 67 km at the northeast corner (north of the Gulf of Papagayo). While the use of a FEM would allow for models that test differing mechanical behaviors of the crustal environment, we chose to hold these constant. By doing so, we can better evaluate differences between this and prior models. Likewise, published results [e.g., *DeShon et al.*, 2006] show little lateral variability in the upper plate structure beneath Nicoya, suggesting that differences would be minimal.

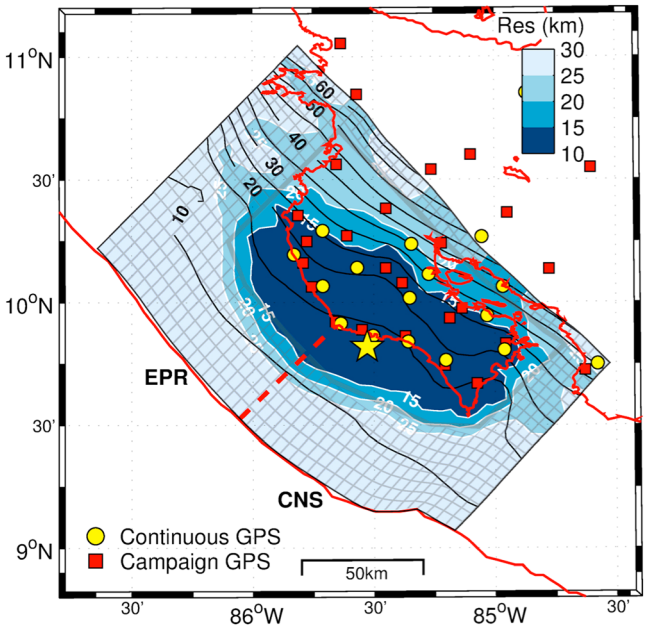

Figure 4. Map of the model resolution spread, *r*, (blue and white contours) for the optimal interseismic solution (described in Figure 6b). Values represent the approximate distance over which an individual interface model element is dependent on neighboring elements. Resolution interdependence for select model elements is shown in Figure S2. The megathrust interface is shown as 5 km black contours [*Kyriakopoulos et al.*, 2015]. Thick gray polygon and hatched area show the high-resolution zone mapped using the checkerboard test in Figure 3a. The red dashed line marks the transition between the subducted extension of the East Pacific Rise (EPR) and Cocos-Nazca Spreading center (CNS) crusts, while the Nicoya Peninsula and Middle America Trench are marked with red solid lines.

To perform benchmark testing against the analytic solutions of *Okada* [1985] and to evaluate geometric fault-specific features in the resultant models, we also create a simplified curviplanar interface model that mimics the analytic model of *Feng et al.* [2012]. The fault is a two-dimensional geometry extending from the trench with a dip of 11°, followed by a progressively steepening dip reaching a maximum of 48° at the Mohorovičić discontinuity, hereafter Moho (Figure S1 in the supporting information). The total domain dimensions of this model are approximately $2200 \times 2200 \times 500$ km with the megathrust interface beneath Nicoya situated near the center. Beneath Nicoya, the model interface is partitioned into 40×29 coincident nodes. The final model comprises approximately 500,000 hexahedral elements, again with higher element density (2.5 km) near the fault (corresponding to a 5 km separation between coincident nodes).

2.2. Resolution Tests

In order to estimate the spatial resolving power of our GPS data and model geometry, we conducted two tests. We performed "checkerboard tests" for each the interseismic (43 stations, Figures 3a and 3b) and coseismic (38 stations, Figures 3c and 3d) GPS networks, highlighting how well we can predict alternating patterns of fault behavior from an initial synthetic model. Likewise, we evaluated the resolution matrix (Figure 4) as obtained through the inverse problem, to identify both the spatial extent to which we can resolve modeled patches and how dependent those patches are on neighboring fault patches (Figure S2).

2.2.1. Checkerboard Tests

Although the two networks have similar spatial coverage we use two different checkerboard inputs based on the spatial extension of interface features we observe in our study. The interseismic locking case (Figure 3a) consists of a finer pattern (4×3 groups of patches) and slip values between 0 and the average interseismic rate of 78.5 mm (equivalent to 100% coupling). In the coseismic case (Figure 3c) we investigate larger asperities (8×4 groups of patches) and slip values which range between 0 and 1 m. The interseismic resolution test (Figures 3a and 3b) shows that both along-strike and along-dip variations in locking are well resolved only beneath the Nicoya Peninsula (above 40 km depth) and extend approximately 20 to 25 km offshore. As expected, resolution decreases dramatically as the model extends farther offshore and toward the trench where land-based geodetic observations are impossible. In the coseismic resolution test (Figures 3c and 3d), input features are also recovered adequately in both along-strike and along-dip directions. Likewise, input slip features are well resolved both below Nicoya and offshore, up to about 25 km from the coast. In the coseismic model, because larger magnitude asperities are easier to recover, the resolution is improved along the deeper interface between 40 and 50 km depth. These two synthetic tests show that resolution is indeed very good beneath Nicoya where the majority of interseismic coupling and coseismic slip were observed but decreases dramatically toward the edges of the fault interface, offshore, and near the trench. For that reason, we focus our discussion on the areas well resolved by our model geometry and data configuration.

2.2.2. Model Resolution Matrix

An additional measure of how well we resolve the slip parameters in our inverse problem can be obtained by exploring the model resolution matrix, defined as $\mathbf{R} = \mathbf{G}^{-g}\,\mathbf{G}$ [*Menke*, 1989], where $\mathbf{G}^{-g}$ is the generalized inverse and $\mathbf{G}$ is the Green's function matrix. For a damped least squares model with weighted data, the solution for $\mathbf{G}^{-g}$ is

$$\mathbf{G}^{-g} = \left(\mathbf{G}^T\mathbf{W}_e\mathrm{G} + \rho \mathrm{W}_m\right)^{-1}\mathbf{G}^T\mathbf{W}_e \tag{1}$$

where $\mathbf{W_e}$ is the error weighting matrix, $\mathbf{W}_m$ is defined by the Laplacian of slip, and ρ is the roughness intensity applied to the model [*Jónsson et al.*, 2002]. In our test we chose to evaluate the preferred interseismic model and its smoothing, described below in section 3.1.

The model resolution matrix is symmetric, with both the columns and rows equal in size to the number of model parameters solved for. If each model parameter were fully resolved and completely independent, the matrix would equal its identity (all diagonals equal 1 and all off-diagonals equal 0). This is rarely the case. Instead, the diagonals are usually less than one, and the off-diagonals on a given row are nonzero and usually positive. This means that for the model parameter defined by that row, the solution of that parameter is dependent on the solution of the other nonzero parameters in that row, with magnitude corresponding to their interdependence. We can describe the spatial interdependence, or spreading of a model parameter, by defining the resolution spread parameter *r* from *Funning et al.* [2005], where the resolution spread for the *i*th model element is

$$r_i = \frac{L_i}{\sqrt{R_i}}, \tag{2}$$

where R_i contains the diagonal elements of $\mathbf{R}$ and L_i represents the patch size. The associated resolution map (Figure 4) shows 10 to 15 km of resolution spread beneath the peninsula, increasing to 25 km farther downdip. Resolution spread remains low and below 15 km for the first 20 km offshore toward the trench, but the spread increases rapidly (resolution diminishes), farther offshore, increasing to greater than 25 km at distances greater than 20–30 km offshore. Not surprisingly, this solution is quite comparable to what is observed through the checkerboard test, as highlighted by the gray bar in Figure 4, which is repeated from Figure 3. To better understand the resolution spread at specific locations on the interface, we also plot a number of individual columns of $\mathbf{R}$, corresponding to individual model patches (Figure S2), also known as "resolution kernels" [*Menke*, 1989, *Funning et al.*, 2007].

2.3. Benchmark Testing

Using the 2-D FEM model described above, we model the interface locking for 15 years of interseismic GPS observations and compare solutions with those from the Okada-based analytic model from *Feng et al.* [2012] using the same data. For our FEM inversions, the linear least squares scheme with positivity and Laplacian smoothing is comparable to that used in *Feng et al.* [2012]. Our benchmark tests show that the numerical solutions are able to reliably reproduce the analytically derived locking in both intensity and pattern (Figure S3), especially below the Nicoya Peninsula, where there is high GPS data density. In particular, the FEM model reproduces the two fully locked patches immediately below and offshore Nicoya, as well as the surrounding locking features present in the analytical solution. Additional results from the benchmark are presented in the supporting information section.

2.4. Interseismic Model

For all models in this study we assume deformation to be purely elastic; and hence, relationship between fault slips and surface deformation can be linearly related. The weighted damped least squares inverse estimated model for deformation due to an assembly of fault patches embedded in an elastostatic domain is

$$\mathbf{m}_{\mathrm{est}} = \mathbf{G}^{-g}\mathbf{d} \tag{3}$$

where $\mathbf{G}^{-g}$ is the generalized inverse defined in (1), $\mathbf{d}$ is a vector of surface displacements, and $\mathbf{m}_{\mathrm{est}}$ the vector of modeled slip parameters [*Menke*, 1989]. For this study, $\mathbf{G}$ is generated using the FEM analysis software ABAQUS (www.simulia.com) to relate the slips to surface displacement through the model geometries described in the previous section [*Kyriakopoulos et al.*, 2013; *Masterlark*, 2003] and then weighted by the smoothed Laplacian of the model fault slip following *Jónsson et al.*, [2002]. To constrain the models, the lateral boundaries and base are fixed to zero displacement.

In the case of the interseismic model, the Green's functions are calculated for each the north, east, and vertical displacements at 43 GPS stations (26 campaign + 17 continuous sites) distributed across and near the Nicoya Peninsula (Figure 3). The vector $\mathbf{m}_{est}$ represents the unknown distribution of back slips, corresponding to "normal" tractions occurring along the fault over time (yielding slipping rates). Here the vector **d** corresponds to the late interseismic velocity field composed of the horizontal and vertical GPS velocities relative to a stable Caribbean plate as defined by *DeMets et al*. [2010].

Following the approach adopted in *Feng et al*. [2012], we initially separate the horizontal velocity field by projecting it onto a local trench-parallel (N45°W) and trench-normal system. While we initially compare the trench-normal solutions for comparisons against those previously published, we also considered the full 3-D motions. To compare against the results of *Feng et al*. [2012], we initially investigate only the trench-normal and vertical velocities.

The inversion algorithm is based on a modification of Occam's regularization scheme [*deGroot-Hedlin and Constable*, 1990], minimizing the chi-square and an additional roughness term to avoid unreasonable oscillations in slip values. We also use the lsqlin Matlab function to imposed bounded constraints for modeled slip. The roughness represents the Laplacian differential of the interface kinematic field multiplied by a weighting factor ρ. During the inversion, the slip values are constrained to vary between zero and the maximum trench-normal convergence rate for the region (V_{norm}). The misfit vector is

$$\mathbf{e} = \mathbf{d} - \mathbf{G}\mathbf{m}_{est} \tag{4}$$

The average uncertainty for the trench-normal horizontal GPS observations is 0.8 mm, while the corresponding uncertainty for the vertical component is 2.5 mm. Although the average error associated with the vertical velocities is 3 times greater than the horizontal one, reducing the weight of the vertical component during the inversion, we chose to include them in the inversion process as an effective constraint to the downdip extension of locking [e.g., *Lundgren et al*., 1999]. The data vector used in the linear inversion is a column vector having 129 (43×3) elements, and the data are weighted according to the reported measurement uncertainties at each station. Finally, we estimate interseismic coupling between the two plates as the ratio of back normal slip rate ($\mathbf{m}_{est}$ vector) to local trench-normal convergence rate ($\mathbf{m}_{est}/V_{norm.}$) [*Savage*, 1983]. For 100% coupling, the back slip would equal the trench-normal convergence rate, with lower values equating to fractional, to zero coupling. The preferred locking distribution is selected from a chi-square versus roughness trade-off analysis [*Jónsson et al*., 2002], where successively increased roughness generates a substantial improvement in chi-square misfits (Figure S4).

While the initial analysis with only trench-normal and vertical motion yields informative results, we find it necessary to incorporate the full 3-D velocity field to best describe the interface behavior, including any trench-parallel coupling that may arise from oblique convergence between the Cocos and Caribbean plates. For this analysis we use the model of *DeMets et al*. [2010] to constrain Cocos-Caribbean motion, finding approximately 78.5 mm/yr (V_{norm}) and 27 mm/yr of trench-normal and trench-parallel motion across the trench striking approximately N45°W. When including the trench-parallel component, we removed 11 mm/yr of northwestward block translation (Figure 1) that was observed across all stations southwest of the Costa Rican volcanic chain [*Feng et al*., 2012], since this motion does not correspond to elastic behavior along the megathrust interface. This reduction leaves a maximum trench-parallel slip rate (V_{lat}) of 16 mm/yr along the megathrust interface. In this case, the model vector and Green's functions matrix are modified to be $\mathbf{m}_{est} = [\mathbf{m}_{dip}, \mathbf{m}_{str}]^{\mathbf{T}}$ and $\mathbf{G} = [\mathbf{G}_{dip}, \mathbf{G}_{str}]$. In the inversion, in addition to constraining the trench-normal "back slip" as before, we too required along-strike motion to remain below V_{lat} (Figure 6).

2.5. Coseismic Model

The procedure for estimating the coseismic slip for the M_w 7.6 2012 Nicoya event is similar to that which we described for the interseismic locking but instead uses *displacement* fields reported in *Protti et al*. [2014] rather than the interseismic *velocity* fields reported in *Feng et al*. [2012]. This displacement field represents a combination of continuous and campaign GPS solutions obtained between 24 h and up to 2 weeks following the event [*Protti et al*., 2014]. Campaign sites in the rupture zone were priorities, having been first

occupied by the field team, so that their solutions represent the smallest early afterslip effects, representing less than about 10% of the coseismic window for this period [*Protti et al*., 2014; *Malservisi et al*., 2015]. The synthetic Green function matrix is generated for both the along-strike and downdip model components ($\mathbf{G} = [\mathbf{G}_{dip}, \mathbf{G}_{str}]$ and $\mathbf{m}_{est} = [\mathbf{m}_{dip}, \mathbf{m}_{str}]^{\mathbf{T}}$) using the same number of patches (43×21) and the same model geometry as the previous section. The displacement observations are collected from 18 continuous and 21 campaign GPS sites totaling 39 GPS coseismic stations [*Protti et al*., 2014]. Thus, the data vector is composed by 117 (39×3) elements including east, north, and vertical displacements. The average uncertainties for the GPS observations are 2.8 mm for horizontal and 7.5 mm for vertical displacements. The inversion results for coseismic slip are presented in Figure 7.

3. Results and Discussion

3.1. Late Interseismic Locking Between 1996 and 2010

We present results for both the initial 2-D geometry of *Feng et al*. [2012] (Figures 5a and 6a) and our new 3-D interface from *Kyriakopoulos et al*. [2015] (Figures 5b and 6b). For both geometries, we include results that either ignore (Figure 5) or retain (Figure 6) trench-parallel GPS, to determine the effect of oblique convergence on overall coupling. In each model, we focus discussion only on areas with high-resolving power as determined by checkerboard tests. For all interseismic models, we can roughly breakdown the interface results into four categories: the fully locked zone with $>90\%$ coupling (red), moderately locked zone with coupling between 50 and 90% (green to orange), the weakly coupled zone between 10 and 50% (blue to cyan), and the freely slipping region with $<10\%$ coupling (magenta).

3.1.1. Comparison of 2-D and 3-D Thrust-Only Locking Models

As expected, the initial FEM result using the 2-D curved interface is nearly identical to the analytical result of *Feng et al*. [2012] using *Okada* [1985], since we used the same data and model geometry. Performing the same analysis using the 3-D geometry of *Kyriakopoulos et al*. [2015], we found comparable but modestly smaller overall misfit (RMS = 2.3 versus 2.4 mm) for similar roughness, $\rho = 5.90$ versus 5.40 mm/km^2. In the new model, the most striking change is that the resolvable fully locked zone in the center of the model became much more focused beneath central Nicoya, in an area just downdip of what would become the nucleation point of the 2012 M_w 7.6 earthquake (yellow star in Figures 5–7). The fully locked zone that protruded offshore in the *Feng et al*., [2012], *Xue et al*. [2015], and our benchmark 2-D models is substantially smaller in our new 3-D model. Because the offshore region is smooth and hence similar to the prior model by *Feng et al*. [2012], we suspect that difference observed here is due to the offshore projection of the locking model beneath land, where the geometry is more complicated.

3.1.2. Comparison of 2-D and 3-D Models for Downdip and Along-Strike Coupling

Given that there was a substantial along-strike component of coseismic slip expected from the 2012 Nicoya earthquake, we created additional models solving for both along-strike and downdip components of coupling for the two model geometries (Figure 6). The first-order location of coupling does not change substantially between these models and the thrust-only ones (Figure 5), with the along-strike component of locking remaining small (rake = 92.5°). The new inversions still require a fully locked patch beneath the central part of Nicoya (coincident with the topographic plateau) and a second fully locked patch immediately offshore the SE corner of the peninsula near the region which ruptured in an earthquake in 1990. Two substantial differences are observed. First, the fully locked patch beneath the central Nicoya is modestly larger in the new models, with most of the increased locking occurring nearer the shallower interface at about 15 km depth. Second, the increased locking here contrasts the region immediately updip and offshore, which now appears to be even less coupled then when the complex geometry alone was introduced (section 3.1.1)—a feature which becomes important when evaluating the rupture zone of the subsequent 2012 earthquake. Overall, implementing the along-strike interseismic velocities and solving for along-strike coupling during the late interseismic period did not affect significantly the locking distribution of the 3-D model. The new locking model that includes both downdip and along-strike behavior along the 3-D interface is our preferred solution (shown in Figure 6b). The RMS values for the 2-D and 3-D models are 2.6 and 2.4 mm for $\rho = 1.46$ versus 1.42 mm/km^2, respectively.

For our best interseismic locking result, we also separate the contribution of along strike versus thrust to our total field for illustration of the individual components (Figure S5). While we found that while the overall locking in the highly resolved area is primarily thrust, as mentioned above, there are two small patches that

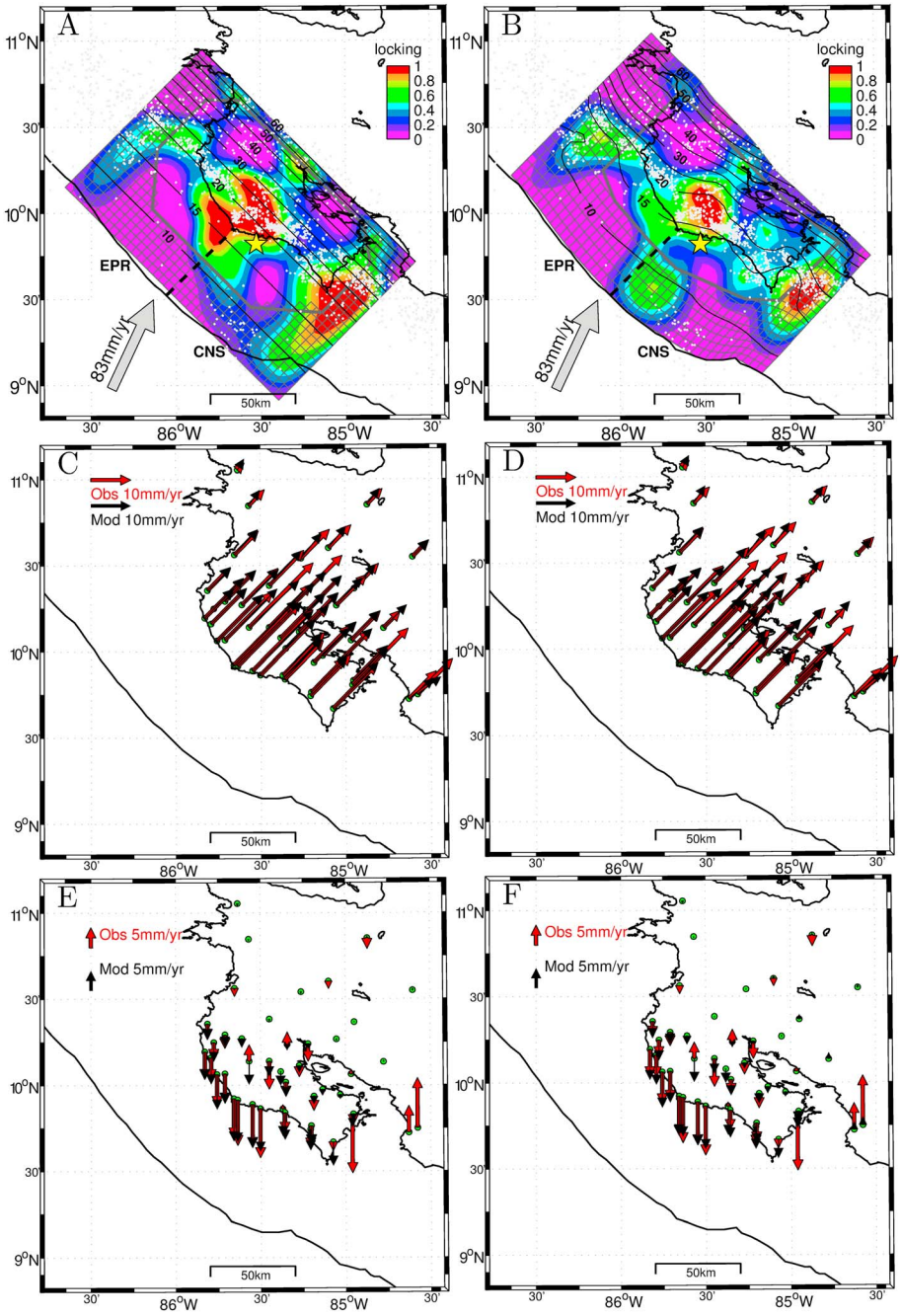

Figure 5. Comparison between (a) two- and (b) three-dimensional interface models of locking for trench-normal and vertical interseismic deformation. Thin black contours show the interface geometries from *Feng et al*. [2012] and *Kyriakopoulos et al*. [2015] for the two- and three-dimensional models, respectively. Large gray vector, in Figures 5a and 5b, show the Cocos plate motion relative to a stable Caribbean plate [*DeMets et al*., 2010]. A yellow star indicates the epicenter for the M_w 7.6 2012 Nicoya earthquake, and gray dots represent interface microseismicity [*Ghosh et al*., 2008]. Thick gray polygons encompass the well-resolved region defined in Figure 3. Comparisons of observed (black arrows) and modeled (red arrows) GPS sites are shown in terms of (c, d) trench-normal and (e, f) vertical components for the models in Figures 5a and 5b, respectively. Exclusion of trench-parallel motion is done for direct comparison to the interseismic coupling model of *Feng et al*. [2012]. The Nicoya Peninsula and Middle America Trench are marked with black solid lines.

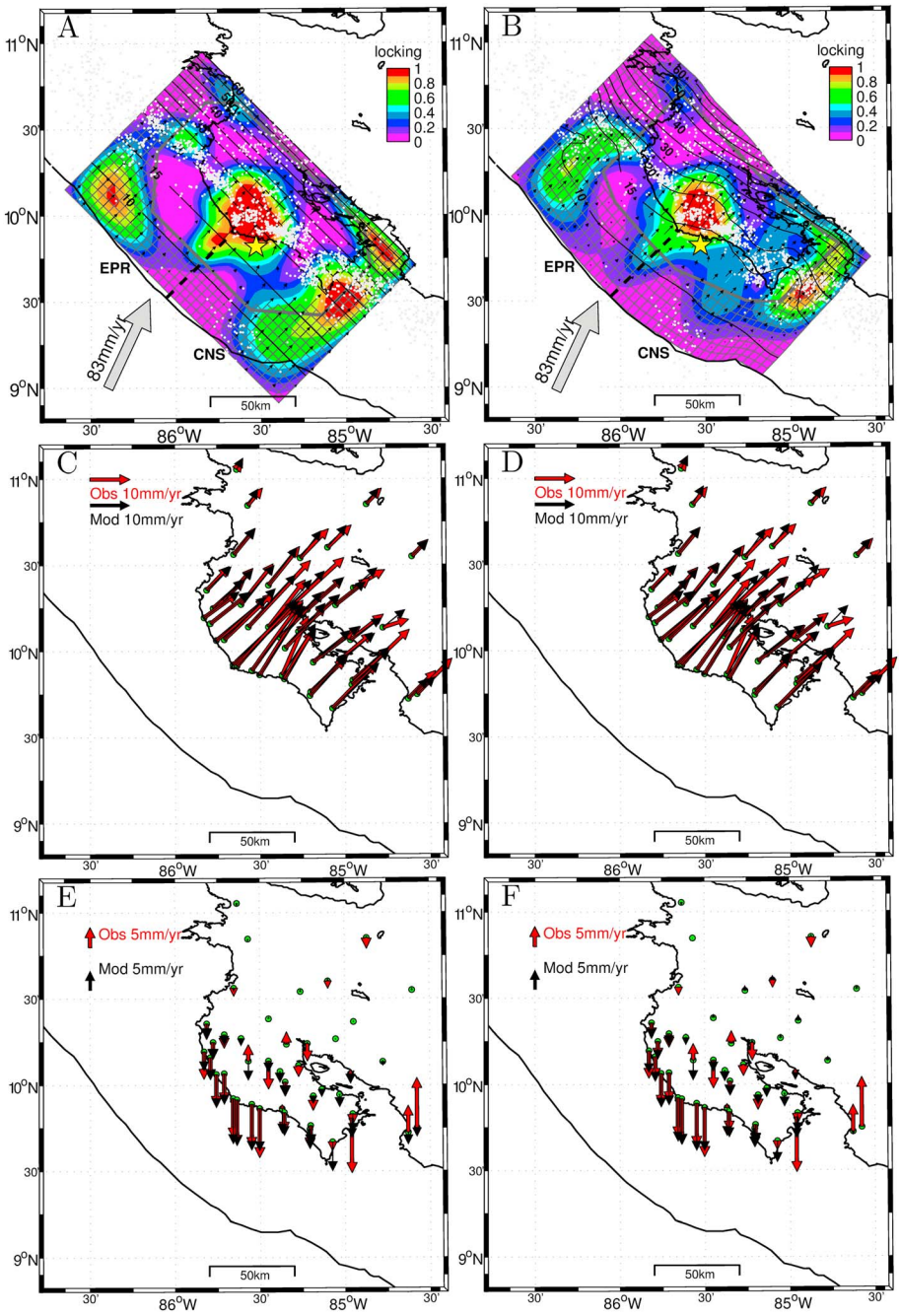

Figure 6. Comparison between (a) two- and (b) three-dimensional interface models of locking for total interseismic deformation field (including trench-parallel motion). Layout and symbols are the same as in Figure 5; however, Figures 6a and 6b also show the vector orientations of upper plate motion (black arrows) and (c, d) include both horizontal components of motion. (e, f) The vertical components of motion.

contribute to along-strike locking, one offshore the southern part of the peninsula and a second coincident with the strongest along-strike locking and the transition between the EPR and CNS crust. This second patch may be explained by the indentation of the elevated CNS crust obliquely colliding into the overriding plate.

3.1.3. General Observations of the Preferred Locking Model

Moderate to fully locked zones (>50%) are mainly concentrated downdip from 15 to 30 km depth in the preferred locking model, coinciding with a narrow band of intense interface microseismicity [*Ghosh et al.*, 2008]. Furthermore, a significant reduction in locking is coincident with the steeping (or bending) of the interface at

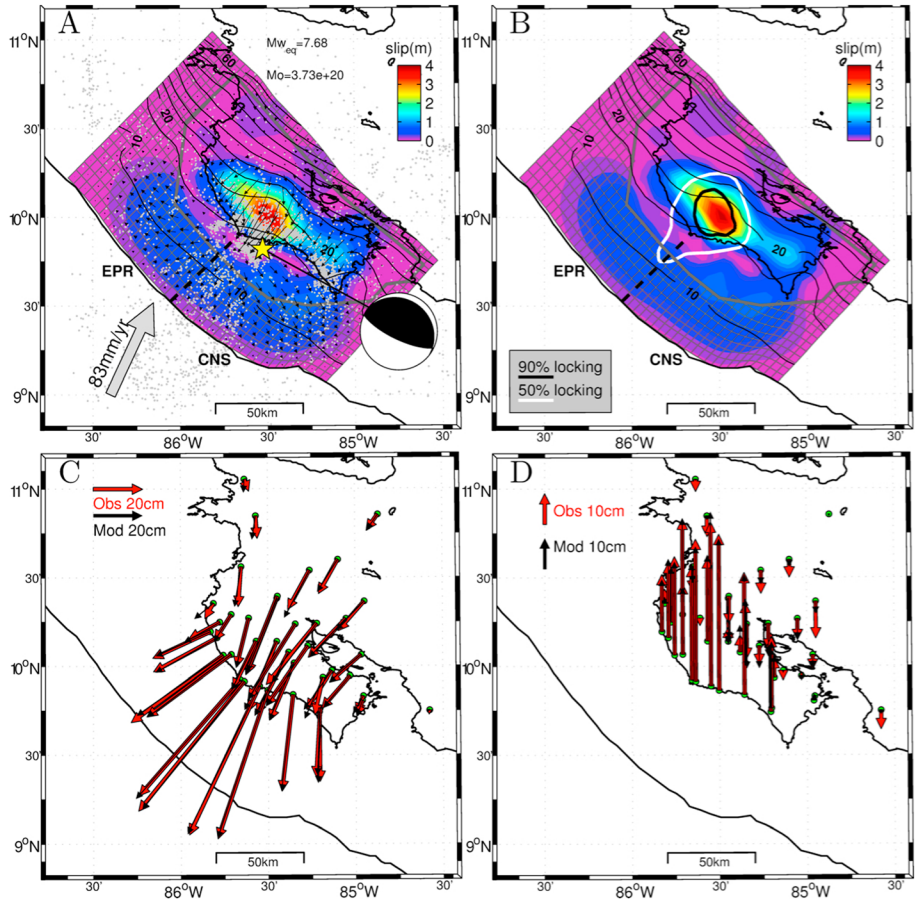

Figure 7. Three-dimensional coseismic slip model for total deformation field observed due to the 2012 Nicoya earthquake. The interface slip model is shown with (a) 3 months of aftershock activity (gray dots) and the vector orientations of coseismic slip (black arrows), and with (b) the estimated locking regions shown in Figure 6b. Here the 50% and 90% locking contours are shown as thick white and black lines, respectively. The global CMT focal mechanism for the 2012 earthquake [*Ekström et al*., 2012] is shown as "beach ball" offset from the event epicenter in Figure 7a. Additional features are the same as in Figures 5 and 6; however, *coseismic displacement* fields are shown as (c) horizontal and (d) vertical components.

approximately 25 km depth and the majority of regional microseismicity (Figure 5b). Contrary to the result of *Norabuena et al*. [2004], and somewhat similar to *Feng et al*. [2012], the interface microseismicity during the interseismic period [*Ghosh et al*., 2008] lies primarily around the updip edge of the locked zone. Interestingly, the near-linear trend of the microseismicity just landward of the coastline extends beyond the strongly locked region in both directions. The reduced offshore seismicity might be the result of low effective stress and inhibition of rupture nucleation as suggested by *Scholz* [1998].

The locked patch beneath central Nicoya coincides geographically with the interface plateau, extending between about 15 and 25 km depth. Immediately updip of the first fully locked patch, offshore of the coastline, there is a moderately locked area (>50% coupling) corresponding to the suture between the EPR and CNS crusts. A second and more poorly resolved fully locked area is offshore the southeastern edge of the peninsula, corresponding to the approximate rupture area of the 1990 M_w 7.3 Gulf of Nicoya earthquake, that occurred at the top the subducted extension of the Fisher seamount chain [*Husen et al*., 2002; *Bilek et al*., 2003; *Kyriakopoulos et al*., 2015]. Because this zone is at the edge of our resolvable region, we exclude further discussion of it here.

Our final optimal solution well describes the distribution of locking beneath the Nicoya Peninsula through the late interseismic period. However, there are a few limitations that must be considered. First, though 3-D, the model ignores any possible spatial variability in the mechanical behavior of the environment. This may have subtle effects on the boundaries and exact location of locking (or slip, as described in the next section). We note, however, that tomographic models of the upper plate beneath the Nicoya Peninsula [*DeShon et al*., 2006;

Moore-Driskell et al., 2013] do not show large-scale changes in the *P* wave or *S* wave velocity structure, other than the topographic change associated the transition between the EPR and CNS crusts. Second, there is a possible but small postseismic contribution from prior earthquakes that may affect our interseismic velocity field. This includes both the M_w 7.7 1950 Nicoya earthquake and the more recent M_w 7.6 1992 Nicaraguan tsunami earthquake. We chose to ignore these events' contributions because their slip parameters are poorly constrained, and their inclusion would hamper our comparison with other studies describe here (none of which included postseismic effects). Finally, most of the GPS data collected in this study were first measured in 2000; thus, the results here best represent the last decade of interseismic coupling. We simply cannot use this data alone to fully predict the total interseismic locking behavior which may change over time due to fault healing, slow-slip events [e.g., *Jiang et al.*, 2012, *Dixon et al.*, 2014], and other earthquake activity in the region.

3.2. Coseismic Slip

Our preferred coseismic slip distribution, using a roughness, $\rho = 50$ mm/km^2 (Figure 7), has a total geodetic moment of 3.73×10^{20} Nm (using a typical crustal rigidity of 30 GPa), corresponding to M_w 7.68 (using the formula of *Hanks and Kanamori* [1979]), similar to the published global CMT solution (3.4×10^{20} Nm; M_w 7.65) [*Ekström et al.*, 2012], and the geodetic moment release modeled by *Protti et al.* [2014] and *Liu et al.* [2015], 3.4×10^{20} Nm and 3.46×10^{20} Nm, respectively. The majority of slip is concentrated beneath the central portion of the Nicoya Peninsula, primarily north and downdip of the earthquake nucleation point or epicenter (shown as a star in Figure 7 and elsewhere). The primary rupture zone extends 90 km along strike beneath Nicoya with an average slip of 0.7 m and roughly confined between the 15 and 25 km depth contour lines. Furthermore, the lateral extension of slip is asymmetrically distributed in relation to the central part of the peninsula and appears to stop at the beginning of the topographic rise beneath the southern end of the peninsula. The geodetically estimated coseismic rake from the highly revolved area is 107°, showing modest right lateral slip. We note this is modestly higher than the gCMT solution of 102° [*Ekström et al.*, 2012] (mechanism shown in Figure 7), due likely to either differences in methodology or modest afterslip inherent in our model. The area of rupture exceeding 2.5 m is approximately 40 km long, while the maximum slip value is about 4.0 m. The high-slip region ($>$2.5 m) coincides with the location of the slab topographic height beneath the central section of Nicoya and immediately downdip of the 2012 main event, between 15 and 20 km depth, somewhat shallower than predicted in the equivalent 2-D model of *Protti et al.* [2014]. Because the Moho appears to intersect the subducted slab near 30 km depth in this area [*DeShon et al.*, 2006], it suggests that the seismogenic downdip limit terminates within the megathrust contact with the upper plate's crust.

An elongated segment of lower slip ($<$1.5 m) continues southeast along the peninsula, representing the only substantial slip zone outside the moderate to strongly locked patches we observed (Figure 6b). This feature is also seen in the *Protti et al.* [2014] and *Liu et al.* [2015] models of coseismic rupture, suggesting that this is not highly dependent on the 3-D nature of the model geometry used here. This elongate feature is not observed in the combined high-rate GPS and seismic inversion model of *Yue et al.* [2013], suggesting that this is an artifact of using temporally delayed campaign GPS data. This feature, however, is not readily observed in the 3 h, afterslip model of *Malservisi et al.* [2015] using the available continuous data, which is limited in resolution in the southern portion of the peninsula, similar to the *Yue et al.* [2013].

The overall shape of the updip edge of the earthquake rupture zone matches both the early aftershock activity from *Protti et al.* [2014] (Figure 7) and the interseismic microseismicity (Figures 5 and 6). The interseismic microseismicity in this region was first defined by *Newman et al.* [2002] as the updip limit of the seismogenic zone; this definition seems to hold true for the coseismic rupture area, as well as the majority of the strongly locked portion of the interface during the interseismic period.

Interestingly, the model also requires some slip offshore and along the near-trench interface shallower than about 10 km depth. This is outside our area of resolution given land-based data and may represent real slip or unconsidered rheologic changes in the near-trench environment. Early aftershocks from *Protti et al.* [2014] primarily occur in the region immediately updip of our modeled coseismic rupture area, mapping out the updip edge of the approximately 1 m slip zone.

3.3. Relation Between Locking and Coseismic Slip Models

Much like what was observed in *Protti et al.* [2014], the high-slip region overlaps substantially with the fully locked area estimated from our interseismic model (Figure 7b). However, the coseismic rupture includes

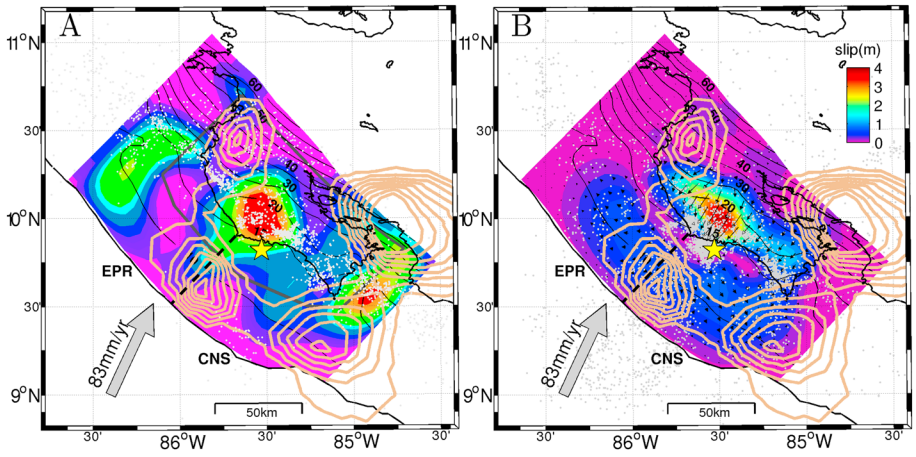

Figure 8. Three-dimensional (a) locking and (b) coseismic slip model for total deformation field observed due to the 2012 Nicoya earthquake in relation to slow-slip events (5 cm beige contours) estimated in *Dixon et al.* [2014]. The total magnitude of modeled slow slip between 2007 and 2012 surrounds the locking and slip regions. Microseismicity is shown in Figure 8a during the late interseismic period (white dots) [*Ghosh et al.*, 2008] and in Figure 8b for the first 3 months of aftershocks (gray dots) from *Protti et al.* [2014]. Other symbols are the same is in Figures 5 through 7.

substantial but lower amplitude slip southeast of the moderately to strongly locked zones. The extension of slip into this region, though required by the GPS reported in *Protti et al.* [2014], may occur coseismically or as very early afterslip. In either case, it appears that the stress perturbation generated along the large slip zone was sufficient to propagate slip into the weak zone here.

In the time since the prior major earthquake in 1950, we estimated that the central segment of the Nicoya locked zone had accumulated sufficient elastic strain to account for the 5 September 2012 megathrust event. From the preferred model (Figure 6b), we estimated the 62 year moment potential (M_{w-62yr}) around the coseismic rupture area. Accounting for only the highly locked region (>90%), we estimated the geodetic locking moment rate of 1.75×10^{18} Nm/yr. If we assume the locking pattern remained constant between the interseismic period, the accumulated moment would be 1.09×10^{20} Nm, equivalent to $M_{w-62yr} = 7.32$, significantly less than released during the 2012 event. However, including the moderately locked region (>50%), the geodetic moment rate is about 3.2 times higher, at 5.61×10^{18} Nm/yr, corresponding to 3.48×10^{20} Nm ($M_{w-62yr} = 7.66$) over 62 years, roughly equivalent to our estimation and the global CMT-determined moment for the 2012 Nicoya. The retrospective analysis done here appears preferable to the one determined prior to the event using the smooth 2-D model in *Feng et al.* [2012], where a moment potential equivalent to an $M_w = 7.8$ was found for the same 62 year period. Our benchmark with comparable roughness using the 2-D model found results similar to *Feng et al.* [2012] and not substantially dependent on our inclusion of along-strike GPS velocities and interface locking. This suggests that the more modest locking solution was primarily due to the change in the interface geometry.

The elastic energy around Nicoya is not released only through coseismic slip or interseismic motion but also through episodic slow-slip events (SSE) with a duration from weeks to months. Seven of these events were detected by a high-precision GPS network in the period from April 2007 through April 2012 [*Dixon et al.*, 2014]. The individual and cumulative SSE's distribution revealed that both the downdip and updip segments of the interface are affected from this episodic phenomenon. Based on the inversion results from *Dixon et al.* [2014], the magnitude of slip is larger at depth (up to 580 mm). The summed slip for the period 2007–2012 provided significant spatial constraints on the extent of both the locked and rupture areas (Figure 8). Indeed, a comparison with our locking map and coseismic slip distribution shows that the modeled SSEs do not penetrate into the fully locked patch beneath the peninsula or the future coseismic rupture. The cumulative SSE map seems to define a clear limit not only the downdip extension of the rupture but also laterally in an area between the structural interface high stand beneath Nicoya and the downdip projection of the fisher seamount. We note that the SSE contours plotted in Figure 8 are from *Dixon et al.* [2014], using the global Slab 1.0 model [*Hayes et al.*, 2012], and not inverted using the new locally defined interface [*Kyriakopoulos et al.*, 2015]. For that reason, details of the SSE distribution edges relative to the locking and rupture models

presented here should not be overinterpreted. Finally, it is possible that our interseismic models, which use a simplified elastic behavior, are somewhat biased by the lack of lateral or downdip heterogeneities [e.g., *Vergne et al*., 2001; *Wang et al*., 2003]. While this may be the case, we suspect its effect is minimal due to the striking colocation of locking with coseismic slip, subducted topography, and microseismicity in the region.

3.4. Subducted Seamounts and Earthquake Rupture

Recently, the role of subducted seafloor topography has become a topic of discussion among earthquake scientists. The increase in data collected around subduction zones (e.g., dense permanent and mobile GPS and seismological networks, ocean bottom seismometers, and offshore geodetic sites) added new and useful constraints on the dynamics of the shallow subduction environment. This has opened new debates on what controls the partitioning and subsequent release of the accumulated seismic moment across the subduction interface. An important question is, How likely is the survival or a subducted protrusion, like a seamount, against friction at seismogenic depths without being "decapitated" along the path or collapse under several GPa of pressure? [e.g., *Watts et al*., 2010]. Results from high-resolution seismic surveys showed that prominent subducted features can be identified down to 25 km depth [*vonHuene et al*., 2000, *Husen et al*., 2002]. In the specific case of the Sumatra subduction zone the preservation depth seems to be even higher. In particular, *Singh et al*. [2011] described a large seamount 40 km wide and 3–4 km high, which appeared to have resisted after 160 km of subduction across the interface to depths of about 40 km. They explained the preservation as the result of weak coupling between the seamount and the upper plate possibly throughout the period of subduction (4 Myr). The above results provide strong evidence for the existence of such features at depth along the interface; however, we do not fully know under what conditions a seamount may be destroyed, and missing from such studies.

Some recent studies show that seamounts are able to modulate both the degree of locking and the rupture process along the plate interface; however, the mechanisms behind the modulation of the seismic cycle are not yet clear. *Scholz and Small* [1997] and later *Bilek et al*. [2003] suggested seamounts act as strong mechanical asperities that accumulate strain during the interseismic period and consequently fail in large earthquakes. However, over the past decade, new data (including high-resolution seismic imaging combined with precise events relocation) have led the scientific community toward the idea of seamounts as "regulators" of the seismic cycle and not just as pure mechanical asperities, meaning that seamounts can act both as earthquake generating asperities or as weakly coupled and continuously creeping patches [*Wang and Bilek*, 2011; *Mochizuki et al*., 2008]. Key to this behavior are how fluids interact along the interface to reduce effective stress as it escapes from the surrounding environment. Widespread fracturing of the upper plate, as a result of mechanical stress associated with the subduction of indenters, will reduce locking across the interface both downdip and near the trench. An example of such interface partitioning may be seen along the northern Chilean seismic gap [*Hayes et al*., 2014, *Schurr et al*., 2014] as well as the rupture area of the 2014 M_w 8.1 Iquique (Chile) earthquake. According to *Geersen et al*. [2015], rupture was limited by subducted seamounts, including a low coupling band at ~20.5°S and preventions of further rupture propagation below 20.5°S. *Yang et al*. [2013] used dynamic rupture simulations to show that subducted seamounts can act as barriers during the actual rupture process, depending on the proximity of rupture nucleation and geometric constraints. These studies provide good evidence to suggest that subducted seamounts modulate the pattern and degree of locking along the plate interface.

In the case of the 2012 Nicoya earthquake, coseismic slip (Figure 7) estimated from our FEM model terminates in its southernmost extent just before the topographic rise interpreted as the downdip extension of the Fisher seamount chain [*Kyriakopoulos et al*., 2015]. Although locking in the area between the two topographic features appears to be low, slip propagated, either as momentum driven slip or as very early afterslip through the weak region, only stopping along strike when hitting the topographic rise. Unfortunately, the static slip imaged here does not allow us to fully explore the role of subducted topography and especially the rupture process. Further dynamic rupture model experiments are likely required to better illuminate the behavior for this particular event.

4. Conclusions

Topographic features of the incoming plate may impart a structural control on the interseismic locking and coseismic slip distribution. Based on a slab model that incorporates these features [*Kyriakopoulos et al*., 2015],

we find that before the 2012 M_w 7.6 Nicoya event, the strongest interseismic coupling was localized beneath the peninsula coincident with an area of high relief along the interface. The locked zone corresponds to an elevated "plateau" of subducted CNS crust immediately southeast of a transition to EPR-generated crust. The same region concentrated the majority of the slip we model during the 2012 earthquake. Our preferred coseismic slip model extends along strike toward the SE edge of the peninsula, immediately downdip of interseismic microseismicity [*Ghosh et al*., 2008] and stopping as it collides into the subducted extent of the Fisher seamount chain, possibly as early afterslip.

Immediately offshore Nicoya, our new 3-D models require substantially less locking prior to the 2012 earthquake, as compared to the model of *Feng et al*. [2012]. The reduced locking, which was focused along the transition between EPR and CNS crust, is important for understanding the total updip potential for earthquake nucleation and tsunami generation. This model now shows that the potential for a large offshore aftershock (estimated up to M_w 6.9 in *Protti et al*. [2014]) was much less likely. According to the new model, the downdip limit of the coseismically determined seismogenic zone is approximately 25 km depth, about 5 km above the megathrust interface with the Moho [*DeShon et al*., 2006].

This work is the starting point for future investigations regarding the modulation of stress around interface topographic features beneath Nicoya and the relationship between the partitioning of locking and geometric complexities [e.g., *Wang et al*., 2007; *Loveless and Meade*, 2010]. The results from this work could be used for future evaluation of the seismic cycle not just along Nicoya, Costa Rica, but could also be applied to subduction zones globally as the community develop more and advanced images of both interseismic locking and coseismic behavior using GPS, seafloor geodesy, and other techniques.

Acknowledgments
The authors are thankful to Mehmet Belkin, Partnership for an Advance Computing Environment (PACE), Georgia Tech, for continuous support with the cluster job scheduling and fine tuning of the computing scripts. Thank you also to J. Dufek and C. Huber for the time and space allocation at the ATLAS supercomputer. Also thank you to Gareth Funning for helpful discussions regarding the resolution matrix. Research is funded through NSF-0847382 and NSF-1447104 to A.V.N. The figures were generated using the Matlab based M_Map (http://www.eos.ubc.ca/~rich/map.html). Optimal interseismic and coseismic model results are available in the 'data products' section of http://nicoya.eas.gatech.edu.

References

Barckhausen, U., C. Ranero, R. von Huene, S. Cande, and H. Roeser (2001), Revised tectonic boundaries in the Cocos Plate off Costa Rica: Implications for the segmentation of the convergent margin and for plate tectonic models, *J. Geophys. Res.*, *106*(B9), 19,207–19,220, doi:10.1029/2001JB000238.

Bilek, S. L., S. Y. Schwartz, and H. R. DeShon (2003), Control of seafloor roughness on earthquake rupture behavior, *Geology*, *31*(5), 455–458, doi:10.1130/0091-7613(2003)031.

deGroot-Hedlin, C., and S. Constable (1990), Occam's inversion to generate smooth, two dimensional models from magnetotelluric data, *Geophysics*, *55*(12), 1613–1624, doi:10.1190/1.1442813.

DeMets, C., R. G. Gordon, and D. F. Argus (2010), Geologically current plate motions, *Geophys. J. Int.*, *181*, 1–80, doi:10.1111/j.1365-246X.2009.04491.x.

DeShon, H. R., S. Y. Schwartz, A. V. Newman, V. Gonzalez, J. M. Protti, L. M. Dorman, T. Dixon, D. E. Sampson, and E. R. Flueh (2006), Seismogenic zone structure beneath the Nicoya Peninsula, Costa Rica, from three-dimensional local earthquake *P*- and *S*-wave tomography, *Geophys. J. Int.*, *164*, 109–124, doi:10.1111/j.1365-246X.2005.02809.x.

Dixon, T. H., Y. Jiang, R. Malservisi, R. McCaffrey, N. Voss, M. Protti, and V. Gonzalez (2014), Earthquake and tsunami forecasts: Relation of slow slip events to subsequent earthquake rupture, *Proc. Natl. Acad. Sci. U.S.A.*, *111*(48), 17,039–17,044, doi:10.1073/pnas.1412299111.

Ekström, G., M. Nettles, and A. M. Dziewonski (2012), The global CMT project 2004-2010: Centroid-moment tensors for 13,017 earthquakes, *Phys. Earth Planet. Inter.*, *200-201*, 1–9, doi:10.1016/j.pepi.2012.04.002.

Feng, L., A. V. Newman, M. Protti, V. González, Y. Jiang, and T. H. Dixon (2012), Active deformation near the Nicoya Peninsula, northwestern Costa Rica, between 1996 and 2010: Interseismic megathrust coupling, *J. Geophys. Res.*, *117*, B06407, doi:10.1029/2012JB009230.

Funning, G. J., B. Parsons, T. J. Wright, J. A. Jackson, and E. J. Fielding (2005), Surface displacements and source parameters of the 2003 Bam, Iran earthquake from Envisat advanced synthetic aperture radar imagery, *J. Geophys. Res.*, *110*, B09406, doi:10.1029/2004JB003338.

Funning, G. J., B. Parsons, and T. J. Wright (2007), Fault slip in the 1997 Manyi, Tibet earthquake from linear elastic modelling of InSAR displacements, *Geophys. J. Int.*, *169*, 988–1008.

Geersen, J., C. R. Ranero, U. Barckhausen, and C. Reichert (2015), Subducting seamounts control interplate coupling and seismic rupture in the 2014 Iquique earthquake area, *Nat. Commun.*, *6*, 1–6, doi:10.1038/ncomms9267.

Ghosh, A., A. V. Newman, A. M. Thomas, and G. T. Farmer (2008), Interface locking along the subduction megathrust from b-value mapping near Nicoya Peninsula, Costa Rica, *Geophys. Res. Lett.*, *35*, L01301, doi:10.1029/2007GL031617.

Hanks, T. C., and H. Kanamori (1979), A moment magnitude scale, *J. Geophys. Res.*, *84*(B5), 2348–2350, doi:10.1029/JB084iB05p02348.

Hayes, G. P., D. J. Wald, and R. L. Johnson (2012), Slab1.0: A three-dimensional model of global subduction zone geometries, *J. Geophys. Res.*, *117*, B01302, doi:10.1029/2011JB008524.

Hayes, G. P., M. W. Herman, W. D. Barnhart, K. P. Furlong, S. Riquelme, H. M. Benz, E. Bergman, S. Barrientos, P. S. Earle, and S. Samsonov (2014), Continuing megathrust earthquake potential in Chile after the 2014 Iquique earthquake, *Nature*, *512*, 295–298, doi:10.1038/nature13677.

Husen, S., E. Kissling, and R. Quintero (2002), Tomographic evidence for a subducted seamount beneath the Gulf of Nicoya, Costa Rica: The cause of the 1990 *Mw* = 7.0 Gulf of Nicoya earthquake, *Geophys. Res. Lett.*, *29*(8), 1238, doi:10.1029/2001GL014045.

Ikari, M. J., A. R. Niemeijer, C. J. Spiers, A. J. Kopf, and D. M. Saffer (2013), Experimental evidence linking slip instability with seafloor lithology and topography at the Costa Rica convergent margin, *Geology*, *41*, 891–894, doi:10.1130/G33956.1.

Jónsson, S., H. Zebker, P. Segall, and F. Amelung (2002), Fault slip distribution of the 1999 M_W 7.1 Hector Mine, California earthquake, estimated from satellite radar and GPS measurements, *Bull. Seismol. Soc. Am.*, *92*(4), 1377–1389, doi:10.1785/0120000922.

Jiang, Y., S. Wdowinski, T. H. Dixon, M. Hackl, M. Protti, and V. Gonzalez (2012), Slow slip events in Costa Rica detectedby continuous GPS observations, 2002–2011, *Geochem. Geophys. Geosyst.*, *13*, Q04006, doi:10.1029/2012GC004058.

Kanamori, H. (1986), Rupture process of subduction-zone earthquakes, *Annu. Rev. Earth Planet. Sci.*, *14*, 293–322.

Kyriakopoulos, C., T. Masterlark, S. Stramondo, M. Chini, and C. Bignami (2013), Coseismic slip distribution for the *Mw* 9 2011 Tohoku-Oki earthquake derived from 3-D FE modeling, *J. Geophys. Res. Solid Earth*, *118*, 3837–3847, doi:10.1002/jgrb.50265.

Kyriakopoulos, C., A. V. Newman, A. M. Thomas, M. Moore-Driskell, and G. T. Farmer (2015), A new seismically constrained subduction interface model for Central America, *J. Geophys. Res. Solid Earth*, *120*, 5535–5548, doi:10.1002/2014JB011859.

Liu, C., Y. Zheng, X. Xiong, R. Wang, A. López, and J. Li (2015), Rupture processes of the 2012 September 5 *Mw*7.6 Nicoya, Costa Rica earthquake constrained by improved geodetic and seismological observations, *Geophys. J. Int.*, *203*(1), 175–183, doi:10.1093/gji/ggv295.

Loveless, J. P., and B. J. Meade (2010), Geodetic imaging of plate motions, fault slip rates, and partitioning of deformation in Japan, *J. Geophys. Res.*, *115*, B02410, doi:10.1029/2008JB006248.

Lundgren, P., M. Protti, A. Donnellan, M. Heflin, E. Hernandez, and D. Jefferson (1999), Seismic cycle and plate margin deformation in Costa Rica: GPS observations from 1994 to 1997, *J. Geophys. Res.*, *104*(B12), 28,915–28,926, doi:10.1029/1999JB900283.

Malservisi, R., et al. (2015), Multiscale postseismic behavior on a megathrust: The 2012 Nicoya earthquake, Costa Rica, *Geochem. Geophys. Geosyst.*, *16*, 1848–1864, doi:10.1002/2015GC005794.

Marone, C. (1998), Laboratory-derived friction laws and their application to seismic faulting, *Annu. Rev. Earth Planet. Sci.*, *26*, 643–696.

Masterlark, T. (2003), Finite element model predictions of static deformation from dislocation sources in a subduction zone: Sensitivities to homogeneous, isotropic, Poisson-solid, and half-space assumptions, *J. Geophys. Res.*, *108*(B11), 2540, doi:10.1029/2002JB002296.

Menke, W. (1989), *Geophysical Data Analysis: Discrete Inverse Theory*, rev. ed., 289 pp., Academic Press, San Diego, Calif.

Mochizuki, K., T. Yamada, M. Shinohara, Y. Yamanaka, and T. Kanazawa (2008), Weak interplate coupling by seamounts and repeating $M \sim 7$ earthquakes, *Science*, *321*(5893), 1194–1197, doi:10.1126/science.1160250.

Montero, W., P. Denyer, R. Barquero, G. Alvarado, and H. Cowan (1998), Map of quaternary faults and folds of Costa Rica, U.S. Geol. Surv. Open File Rep., 98-0481.

Moore-Driskell, M., H. R. DeShon, W. Rabbel, M. Thorwart, Y. Dzierma, and I. G. Arroyo (2013), Integration of arrival-time datasets for consistent quality control: A case study of amphibious experiments along the Middle America Trench, *Bull. Seismol. Soc. Am.*, *103*(5), 2752–2766, doi:10.1785/0120120274.

Newman A. V., S. Y. Schwartz, V. González, H. R. DeShon, J. M. Protti, and L. M. Dorman (2002), Along-strike variability in the seismogenic zone below Nicoya Peninsula, Costa Rica, *Geophys. Res. Lett.*, *29*(20), 1977, doi:10.1029/2002GL015409.

Norabuena, E., et al. (2004), Geodetic and seismic constraints on some seismogenic zone processes in Costa Rica, *J. Geophys. Res.*, *109*, B11403, doi:10.1029/2003JB002931.

Okada, Y. (1985), Surface deformation due to shear and tensile faults in a half-space, *Bull. Seismol. Soc. Am.*, *75*, 1435–1154.

Protti, M., M. F. Güendel, and E. Malavassi (2001), *Evaluación del Potencial Sísmico de la Península de Nicoya*, 1st ed., 144 pp., Ed. Fund. Univ. Nac., Heredia, Costa Rica.

Protti, M., V. González, A. V. Newman, T. H. Dixon, S. Y. Schwartz, J. S. Marshall, L. Feng, J. I. Walter, R. Malservisi, and S. E. Owen (2014), Nicoya earthquake rupture anticipated by geodetic measurement of the locked plate interface, *Nat. Geosci.*, *7*, 117–121, doi:10.1038/ngeo2038.

Savage, J. (1983), A dislocation model of strain accumulation and release at a subduction zone, *J. Geophys. Res.*, *88*(B6), 4984–4996, doi:10.1029/JB088iB06p04984.

Scholz, C. H. (1998), Earthquakes and friction laws, *Nature*, *391*, 37–42, doi:10.1038/34097.

Scholz, C. H., and C. Small (1997), The effect of seamount subduction on seismic coupling, *Geology*, *25*(6), 487–490, doi:10.1130/0091-7613.

Schurr, B., et al. (2014), Gradual unlocking of plate boundary controlled initiation of the 2014 Iquique earthquake, *Nature*, *512*(7514), 299–302, doi:10.1038/nature13681.

Singh, S. C., et al. (2011), Aseismic zone and earthquake segmentation associated with a deep subducted seamount in Sumatra, *Nat. Publishing Group*, *4*(5), 308–311, doi:10.1038/ngeo1119.

Vergne, J., R. Cattin, and J. P. Avouac (2001), On the use of dislocations to model interseismic strain and strain build-up at intercontinental thrust faults, *Geophys. J. Int.*, *147*, 155–162.

vonHuene, R., C. R. Ranero, W. Weinrebe, and K. Hinz (2000), Quaternary convergent margin tectonics of Costa Rica, segmentation of the Cocos Plate, and Central American volcanism, *Tectonics*, *19*(2), 314–334, doi:10.1029/1999TC001143.

Wang, K., and S. L. Bilek (2011), Do subducting seamounts generate or stop large earthquakes?, *Geology*, *39*, 819–822, doi:10.1130/G31856.1.

Wang, K., R. Wells, S. Mazzotti, R. D. Hyndman, and T. Sagiya (2003), A revised dislocation model of interseismic deformation of the Cascadia subduction zone, *J. Geophys. Res.*, *108*(B1), 2026, doi:10.1029/2001JB001227.

Wang, K., Y. Hu, M. Bevis, E. Kendrick, R. J. Smalley, R. B. Vargas, and E. Lauría (2007), Crustal motion in the zone of the 1960 Chile earthquake: Detangling earthquake-cycle deformation and forearc sliver translation, *Geochem. Geophys. Geosyst.*, *8*, Q10010, doi:10.1029/2007GC001721.

Watts, A. B., A. A. P. Koppers, and D. P. Robinson (2010), Seamount subduction and earthquakes, *Oceanography*, *23*(1), 166–173.

Xue, L., S. Schwartz, Z. Liu, and L. Feng (2015), Interseismic megathrust coupling beneath the Nicoya Peninsula, Costa Rica, from the joint inversion of InSAR and GPS data, *J. Geophys. Res. Solid Earth*, *120*, 3707–3722, doi:10.1002/2014JB011844.

Yang, H., Y. Liu, and J. Lin (2013), Geometrical effects of a subducted seamount on stopping megathrust ruptures, *Geophys. Res. Lett.*, *40*, 2011–2016, doi:10.1002/grl.50509.

Yue, H., T. Lay, S. Y. Schwartz, L. Rivera, M. Protti, T. H. Dixon, S. Owen, and A. V. Newman (2013), The 5 September 2012 Nicoya, Costa Rica *Mw*7.6 earthquake rupture process from joint inversion of high-rate GPS, strong-motion, and teleseismic *P* wave data and its relationship to adjacent plate boundary interface properties, *J. Geophys. Res. Solid Earth*, *118*, 5453–5466, doi:10.1002/jgrb.50379.

Journal of Geophysical Research Solid Earth

Supporting Information for

Structural Asperity focusing locking and earthquake slip along the Nicoya megathrust, Costa Rica.

C. Kyriakopoulos[1] and A.V. Newman[2]

[1]University of California, Riverside, Department of Earth Sciences.

[2]Georgia Institute of Technology, School of Earth and Atmospheric Sciences.

Contents of this file

Figures S1 to S5

Introduction

The supporting information consist of five figures. **Figure S1** (in section 2.1) provides a global view of the finite element models presented in this paper. **Figure S2** (in section 2.2) shows the resolution kernels from the fault interface**. Figure S3** (in section 2.3) shows the comparison between analytical and finite element based solutions. **Figure S4** (in section 2.4) shows up-dip locking for the 3D interface (topographic) for different values of roughness. **Figure S5** (in section 3.1.2) shows the up-dip and along strike components of locking for our preferred model.

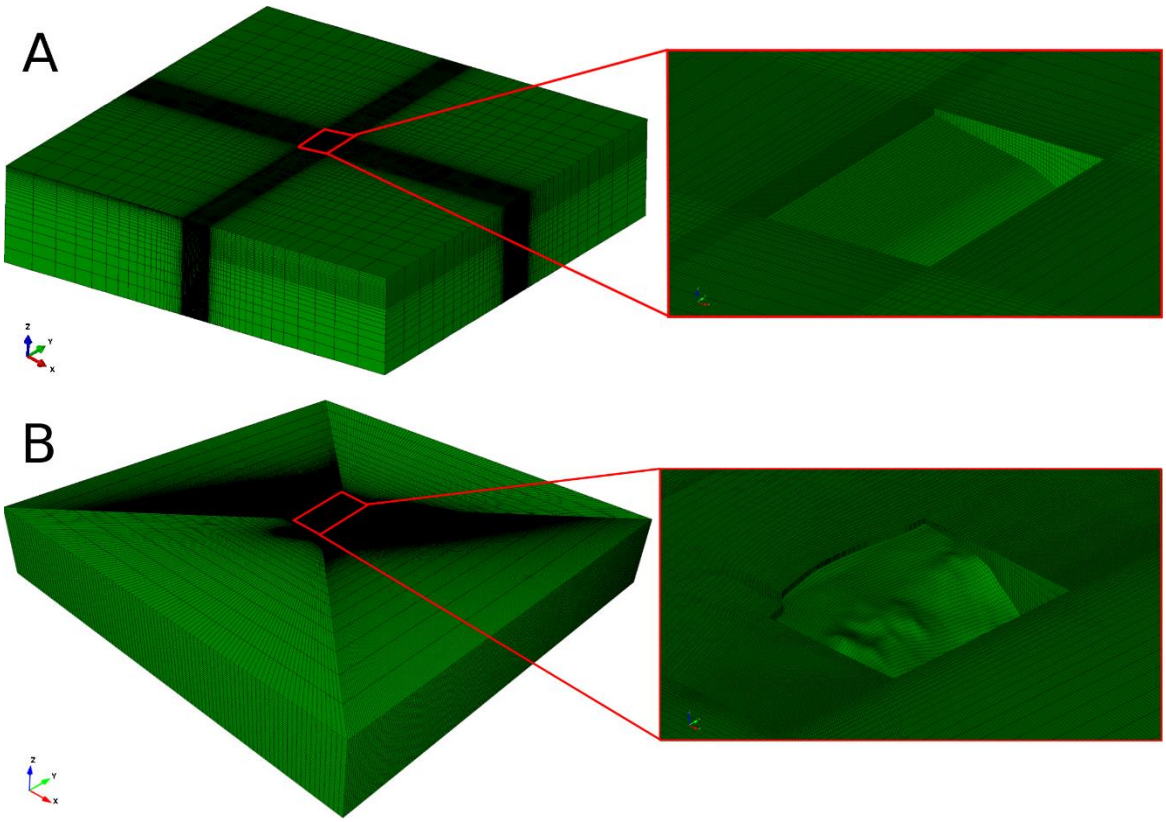

Figure S1. Full Finite Element (FE) mesh for the (**A**) two-dimensional and (**B**) three-dimensional interface models. The exposed interface below the Nicoya Peninsula is detailed in the pop-out images (a flat-surfaced upper-plate is removed for visibility).

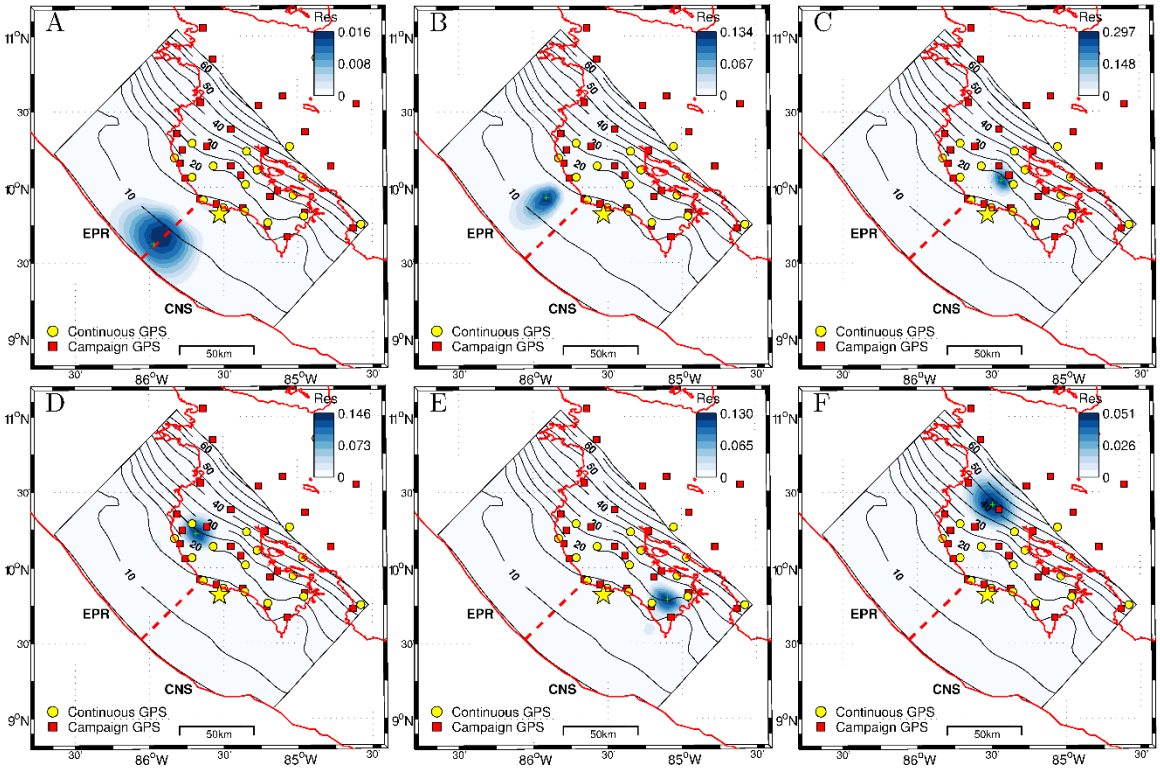

Figure S2. Resolution kernels (columns of matrix **R**; blue color map) for our preferred interseismic locking model **(Figure 6b**) for six locations across the model interface: **A)** Offshore and near trench kernel; **B)** Offshore kernel near the coastline; **C)** Kernel imemdiately beneath the peninsula and coincident with topographic rise and fully locked zone; **D)** and **E)** kernels imemaditely NW and SE of location **(C)**; **F)** downdip of locked zone. The blue area covered by each kernel is an indication of the resolution spread of a particular locking feature, identifying the minimum size of a feature we can resolve along the interface at a particular location. Note that the color scale is plot-dependent for clarity. The red dashed line marks the transition between the subducted extension of the East Pacific Rise (EPR) and Cocos-Nazca Spreading Center (CNS) crusts, while the Nicoya peninsula and Middle America Trench are marked with red solid lines. A small green cross indicates the approximate center of each fault patch illustrated (**A – F**).

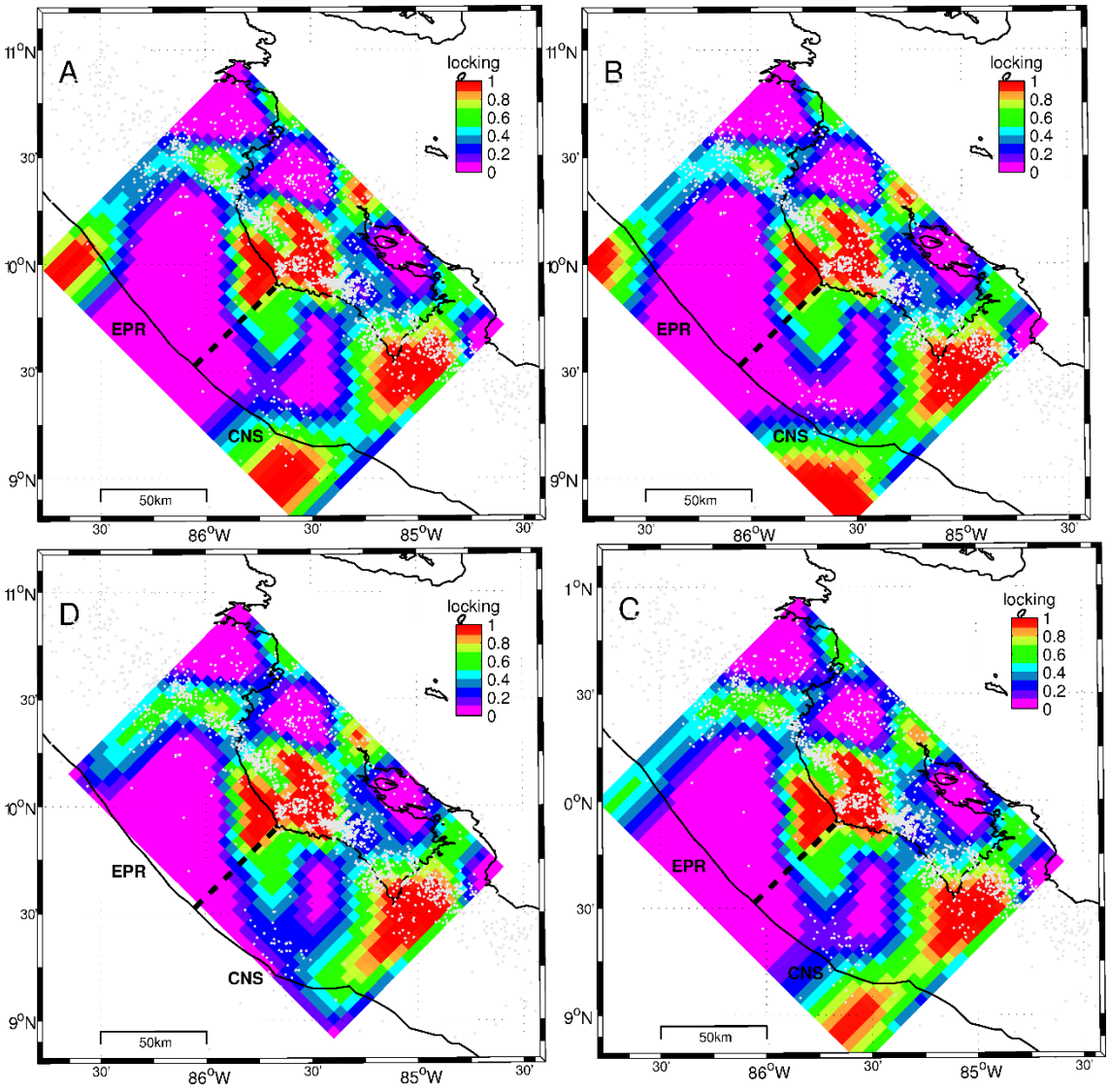

Figure S3. Benchmark testing of analytic and Finite-Element (FE) interseismic locking models. **(A)** The analytical solution of Okada (1992) is shown for the results published in *Feng et al.* (2012). This appears almost identical to the equivalent (**B, C**) FE models using ABAQUS and linear constraint equations for larger or smaller elements immediately offshore the trench, respectively. The same model is also shown (**D**) without a post-trench seaward extension, that is normally included in our flat-surface geometry. The black dashed line marks the transition between the subducted extension of the East Pacific Rise (EPR) and Cocos-Nazca Spreading Center (CNS) crusts. The Nicoya peninsula and Middle

America Trench are marked with black solid lines. Gray dots represent interface microseismicity (*Ghosh et al.*, 2008).

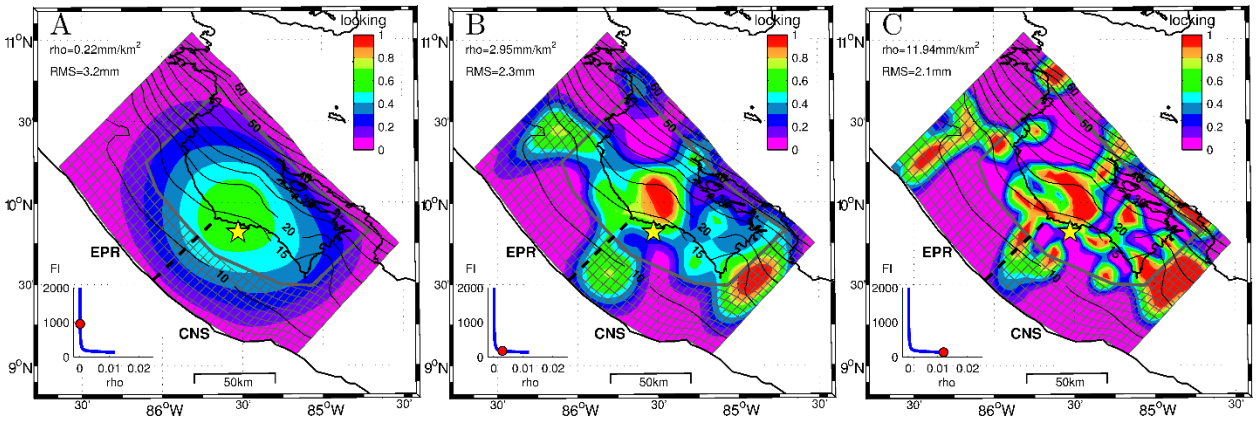

Figure S4. Comparison of estimated interseismic locking solutions with differing interface slip roughness using our three-dimensional interface model. The figure presents the sensitivity of the estimated locking to the increasing roughness (ρ) coefficients going from (**A** to **C**). Solutions with increased roughness (decreased smoothness) allow for much improved fit to data. Inset plots show the position (red dots) along-the misfit-roughness curves for the individual cases. Symbols are the same as in **Figures 4-7** of the main text.

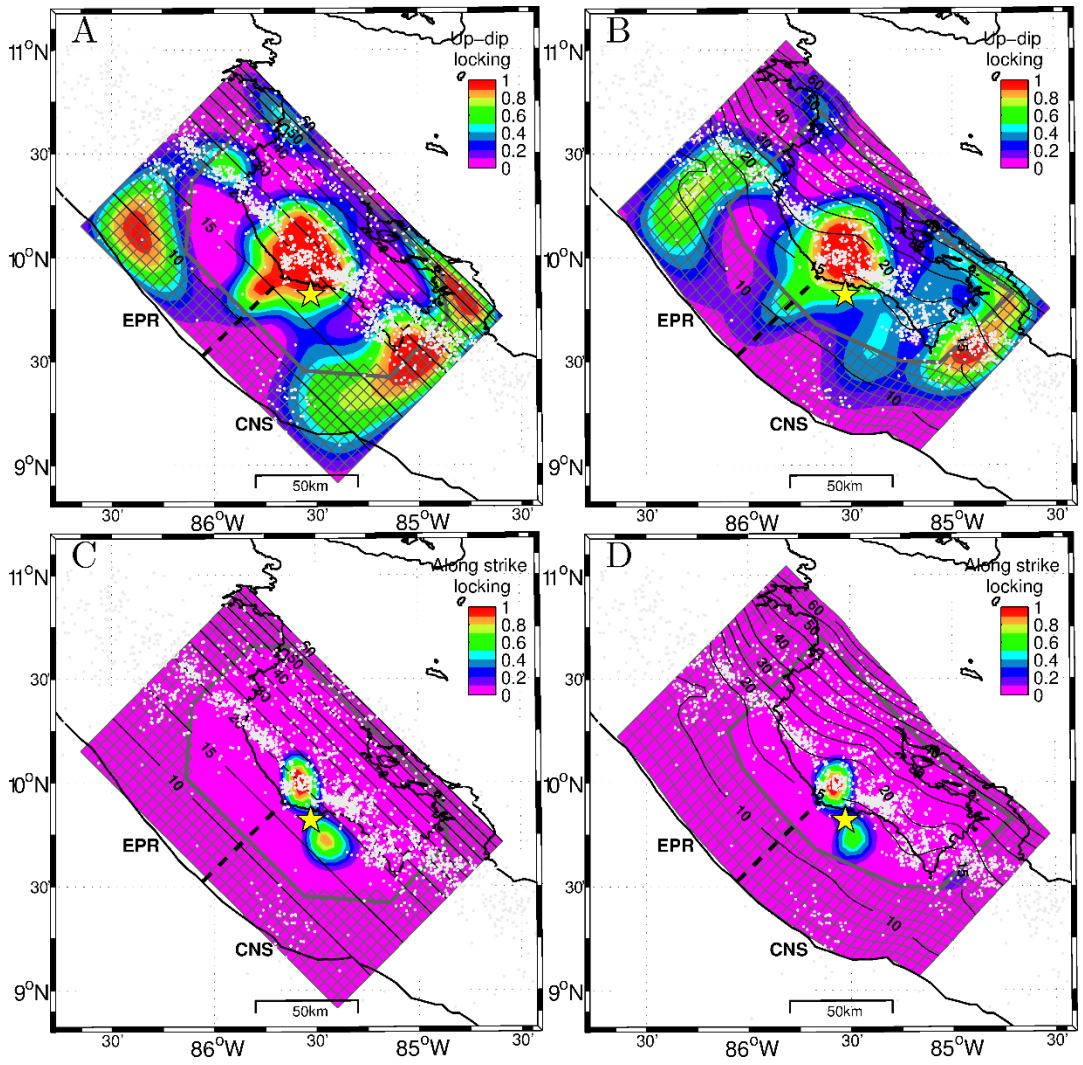

Figure S5. Selected Interseismic locking model. Comparison between up-dip **(A, B)** and along strike locking models **(C, D)** for the full interseismic deformation field (including trench-parallel motion). The Nicoya peninsula coastline and the oceanic trench are represented with a black line.